AJNR

Magnetic Resonance Properties of Hydrogen: Imaging the Posterior Fossa

I. R. Young, M. Burl, G. J. Clarke, A. S. Hall, T. Pasmore, A. G. Collins, D. T. Smith, J. S. Orr, G. M. Bydder, F. H. Doyle, R. H. Greenspan and R. E. Steiner

Magnetic Resonance Properties of Hydrogen:
Imaging the Posterior Fossa

I. R. Young[1]
M. Burl[1]
G. J. Clarke[1]
A. S. Hall[1]
T. Pasmore[1]
A. G. Collins[1]
D. T. Smith[1]
J. S. Orr[2]
G. M. Bydder[2]
F. H. Doyle[2]
R. H. Greenspan[2, 3]
R. E. Steiner[2]

Posterior fossa scans were performed on five healthy volunteers using a nuclear magnetic resonance (NMR) machine constructed by Thorn-EMI Ltd. Three different NMR scanning sequences were used. In the first, a type of saturation-recovery technique was used to produce images strongly dependent on the density of hydrogen nuclei, but with some dependence on the spin-lattice relaxation time (T_1). In the second, an inversion-recovery technique was used to produce images with a stronger dependence on the spin-lattice relaxation time. In the third, a spin-echo technique was used to obtain images with a dependence on the spin-spin relaxation time (T_2). All three types of NMR image were unaffected by bone artifact. Visualization of brain adjacent to the skull base was obtained without loss of detail due to partial-volume effect from bone.

The saturation-recovery images highlighted arteries and veins that were clearly visible without the use of contrast agents. The inversion-recovery images showed remarkable gray-white matter differentiation enabling internal structure to be seen within the brainstem and cerebellum. The trigeminal nerve and ganglion were also seen outside the brain. Experience with the spin-echo technique is limited, but the images at the base of the brain show considerable soft-tissue detail. The NMR images of the posterior fossa in this study were comparable in quality to those obtained from a new rotate-rotate x-ray computed tomography machine and were superior in several respects.

The introduction of x-ray computed tomography (CT) nearly 10 years ago revolutionized the practice of neuroradiology. Since then, CT technology improvements as well as the use of intravenous and cisternal contrast agents have extended the role of CT which now occupies a preeminent position in imaging of the brain. CT scanning of the posterior fossa, however, has always been less satisfactory than in the supratentorial compartment principally because of artifacts from surrounding bone.

The development of imaging systems using the magnetic resonance properties of hydrogen, in which bone gives a low intensity signal, offers an advantage in areas in which bone artifact poses a problem with CT. In addition, nuclear magnetic resonance (NMR) images can be produced using several different scanning sequences. These reflect, to varying degrees, the density of mobile hydrogen nuclei and the rates at which hydrogen nuclei exchange energy with themselves or lose energy to their molecular environment.

The first images of the brain produced at the Central Research Laboratories of Thorn-EMI Ltd. were obtained with an NMR machine based on a resistive magnet in 1978 [1]; since then, several groups have published images produced with different NMR techniques [2–8]. We illustrate the use of three different NMR techniques for imaging the posterior fossa and base of the brain using an NMR machine based on a cryomagnet, and we compare the results with CT.

Subjects and Methods

With permission from the Ethical Committee of the Royal Post-graduate Medical School, five normal volunteers aged 27–63 years (three male, two female) were scanned. All examinations conformed to the guidelines provided by the National Radiological Protection Board [9]. Two of the volunteers also had CT scans of the posterior fossa performed on a 1981 model Siemens Somatom 2 whole body scanner. CT scans of 10 sec were obtained at 125 kVp using the head mode of this machine.

NMR Scanner Operation

The NMR scanner was constructed by Thorn-EMI Ltd and is capable of performing several different scanning sequences. For all examinations, the patient lies in the central aperture along the axis of a cylindrical liquid-helium-cooled superconducting magnet made by Oxford Instruments Ltd., which produces a uniform static magnetic field (H_0) of 1,500 gauss (0.15 tesla). This magnetic field produces a net alignment of nuclear magnetic dipoles in the direction of the field (fig. 1).

A transmitter coil around the patient's head produces a 6.5 MHz electromagnetic field corresponding to the proton resonant frequency for the H_0 field strength (fig. 1). The electromagnetic field is used to perturb the equilibrium distribution of protons (fig. 2), where a so-called 90° radiofrequency (RF) pulse is used to rotate the net magnetization along the +Z axis through 90° into the XY plane. After such a pulse, the protons slowly return to their previous lower energy equilibrium state by reradiating RF energy which is detected by a receiver coil as an induced electrical signal.

To select a slice and produce a two-dimensional image, spatial discrimination is provided by magnetic field gradients. During the RF 90° pulse, a changing magnetic field gradient is applied in the Z direction, so that the total magnetic field outside the required slice is either too high or too low for the nuclei to fulfill the resonant condition with the applied RF field. Gradient fields are also applied in the X and Y directions producing a radial (R) gradient in order to spatially encode the signal by altering proton resonant frequencies within the slice. Views of the patient are taken in 1° steps for 180° by altering the R gradient. The cross-section is reconstructed by a Fourier transform of each angle, followed by back-projection. Slice thickness is about 9 mm and images are displayed on a 256 × 256 matrix with a pixel size of less than 2.5 mm².

The processing time for the published scan was 4 min, but it is now less than 1 min. Each sequence requires a separate scan which the operator chooses at the beginning of the examination.

Relaxation Mechanisms

After a 90° RF pulse, the magnetization returns or relaxes to equilibrium in the +Z direction. This relaxation, which is characterized by the time constant T_1, is known as the "spin-lattice" relaxation and describes the tendency for nuclei to lose energy to surrounding nuclei, realigning the net magnetization into the +Z direction. This process is due to interaction caused by the thermal movement of the protons and the other nuclei round them.

Spin-spin relaxation, which also occurs after a 90° RF pulse, is due to local field inhomogeneities causing individual hydrogen nuclei to precess at different rates so they become progressively out of phase, resulting in a reduction in the net magnetization in the XY plane. This process is characterised by the time constant T_2. Since spin-spin relaxation mechanisms include all the spin-lattice interactions plus additional relaxation processes, T_2 is always less than or equal to T_1. Both relaxation processes are approximately exponential for homogeneous samples.

Saturation-Recovery Sequence

In the saturation-recovery sequence (fig. 2), single 90° RF pulses are used for each of the 180 projections. If the repetition time between successive projections is sufficiently long for the magnetization vector to be realigned completely from the XY plane to the +Z direction, the measured signal has no significant T_1 or T_2 dependence. This usually requires at least 1 sec between 90° RF pulses. When the repetition time is shortened and becomes similar to T_1, there is only partial recovery of the magnetization along the +Z direction, so that the following RF pulse rotates a reduced magnetization vector through 90°, leading to a smaller induced signal. Consequently, when a short repetition time is used, tissues or fluid with a relatively long T_1 such as cerebrospinal fluid give a low signal and appear dark. Tissues such as cortical bone also give a low signal and appear dark, but this is due to their low hydrogen content.

An exception to the pattern of reduced signal due to reduced repetition time arises in the case of flowing blood. Although blood has a long T_1 and might be expected to appear dark, blood that flows into the slice between pulses will not have experienced any previous disturbance by the RF. It thus appears to have fully recovered, as though it were a material with a short T_1, and gives a high signal, appearing white.

Inversion-Recovery Sequence

In the inversion-recovery scanning mode (fig. 3), initially a 180° RF pulse is applied inverting the magnetization vector from the +Z direction to the −Z direction. After some period τ, a 90° pulse is applied rotating the residual magnetization into the XY plane, after which an induced signal is obtained as in the saturation-recovery sequence. If T_1 is short compared to τ, the spin-lattice relaxation mechanisms will have returned the nuclei to their initial equilibrium distribution. However, if T_1 is comparable to τ, there will be a reduced component of magnetization in the +Z direction when the 90° pulse is applied and, consequently, a lower detected signal. In this sequence, tissues with a short T_1 appear lighter than tissues with a long T_1.

Spin-Echo Technique

The spin-echo sequence (fig. 4) produces images from an echo signal the size of which, relative to the initial signal, is
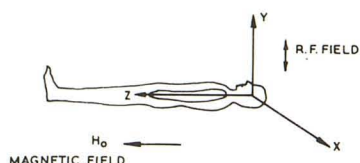

Fig. 1.—Orientation of patient to magnetic fields. Patient lies inside cylindrical magnet producing uniform magnet field H_0 in +Z direction. Transmitter coil around head produces radiofrequency electromagnetic field changing in the ± Y direction.
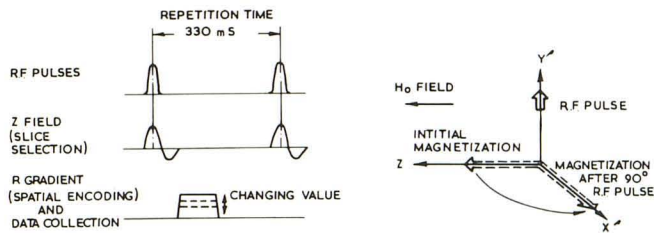
Fig. 2.—Saturation-recovery sequence. One cycle of applied sequence of magnetic fields with corresponding changes in magnetization vector in rotating frame of reference, X', Y', Z. A 90° RF pulse in orientation shown in direction Y' rotates magnetization from +Z to +X direction. While magnetization is recovering along +Z axis, radial (R) gradient is applied to produce spatial encoding and data is collected. Direction of the R gradient is changed by 1° interval to collect total 180 projections. Pulsed Z field provides slice selection.
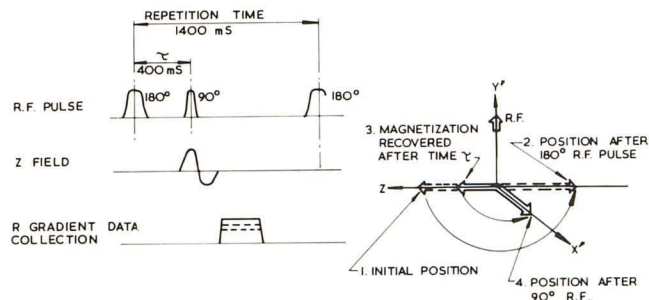

Fig. 3.—Inversion-recovery sequence. One cycle, period 1400 msec, of applied sequence of magnetic fields. Vector diagram illustrates magnitude and direction of magnetization. A 180° RF pulse inverts vector from along +Z direction to −Z direction. After time period τ of 400 msec, during which some degree of recovery of magnetization along +Z direction occurs, a 90° RF pulse is applied which rotates vector along X' axis. Spatial encoding signal recovery and slice selection then proceed as for saturation-recovery sequence.
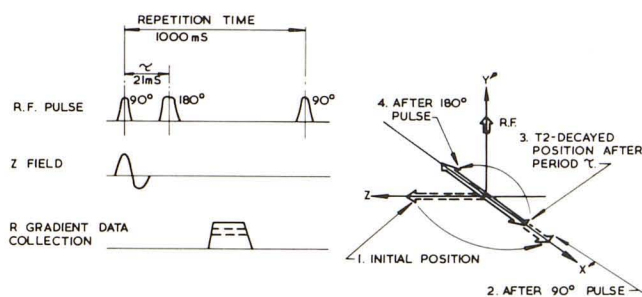

Fig. 4.—Spin-echo sequence. Sequence of applied magnetic fields and behavior of net magnetization vector. A 90% pulse is used to rotate vector from initial position (1) along +Z axis to position in X'Y' plane along X' axis (2). During period τ, vector decreases due to dephasing as described in text (3). Then 180° RF pulse is applied to rotate vector through −Z axis back into X'Y' plane (4). After further time τ, rephased echo signal is obtained when R gradient is applied.

strongly dependent on T_2 [10]. Initially a 90° RF pulse rotates the magnetization vector into the XY plane where spin-spin interactions reduce the size of the vector due to dephasing as described above. Usually a lack of homoge-

neity in the H_0 field adds to the local inhomogenities speeding up the dephasing process.

If after a period τ, a 180° RF pulse is applied, and all the components of the magnetization vector in the XY plane are rotated through the −Z axis back into the XY plane. This reverses their relative orientations, and some of the different rates of precession that were causing dephasing now have the opposite effect causing a rephasing. After a further identical time τ, some of the components realign and a rephasing signal appears giving the so-called echo. Because the effects of H_0 defects cancel out and do not reduce the strength of the rephased signal, the technique is very tolerant to imperfections in H_0. τ is chosen much smaller than T_1, so very little recovery occurs along the +Z direction. The echo signal is then smaller than the initial signal due to the T_2 relaxation processes. In this sequence, for instrumental reasons, tissues with a short T_2 appear darker than those with a long T_2.

Results

Saturation-recovery pictures of the brain show a general similarity to CT, but differ strikingly in clearly demonstrating arteries, vein, and venous sinuses particularly within and adjacent to bone. The outstanding feature of the inversion-recovery pictures is the marked differentiation between gray and white matter, enabling internal structure within the brainstem, cerebellum, and spinal cord to be visualized. The spin-echo scans of the brain display little contrast between gray and white matter, although differences in soft-tissue detail at the base of the brain are apparent.

With all three types of NMR image, less linear artifact is seen than with CT enabling the margins of the brainstem, cerebellum, and spinal cord to be seen. However, small central artifacts are often seen with NMR. Details of scans at specific levels are presented below.

Comparable CT, inversion-recovery, and spin-echo scans of the mesencephalon in the same subject are shown in figure 5. The inversion-recovery scan shows considerable differentiation between gray and white matter within the frontal temporal and occipital lobes. The white matter is visible to subcortical level and the gyrus recti are seen within the frontal lobes on either side of the midline. The anterolateral aspects of the frontal lobes are also seen unobscured by partial-volume effect from the floor of the anterior fossa. The margins of the mesencephalon are clearly defined on the NMR scan and the basis pedunculi and substantia nigra are visible within the brainstem. The spin-echo scan displays little contrast between gray and white matter, but the optic chiasm is seen with the internal carotid arteries placed laterally on either side. A central artifact is seen adjacent to the left inferior colliculus.

Comparable CT, saturation-recovery, and inversion-recovery scans of the upper pons in another subject are shown in figure 6. The fourth ventricle and part of the superior cerebellar cistern are visible in all three images (see fig. 6D). The saturation-recovery scan shows the fourth ventricle and margins of the brainstem and cerebellum with greater clarity than CT. The temporal lobe is also seen within
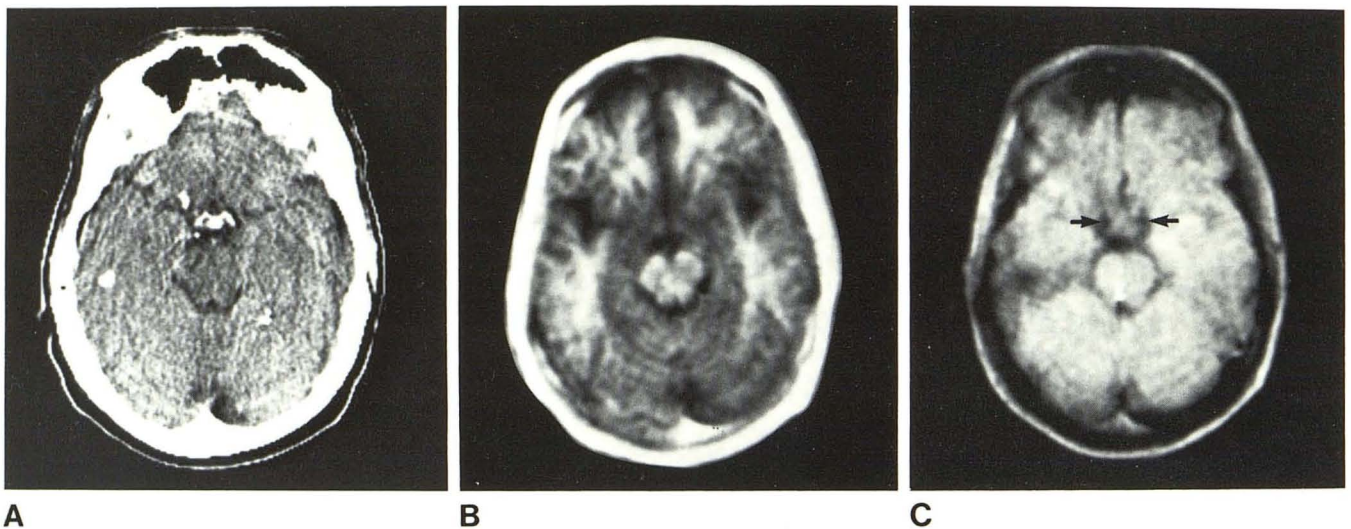
A

B

C

Fig. 5.—CT (**A**), inversion-recovery (**B**), and spin-echo (**C**) scans of mes-
encephalon. White rim on CT scan due to bone; on NMR scans due to
subcutaneous fat and yellow bone marrow. Internal carotid arteries seen on
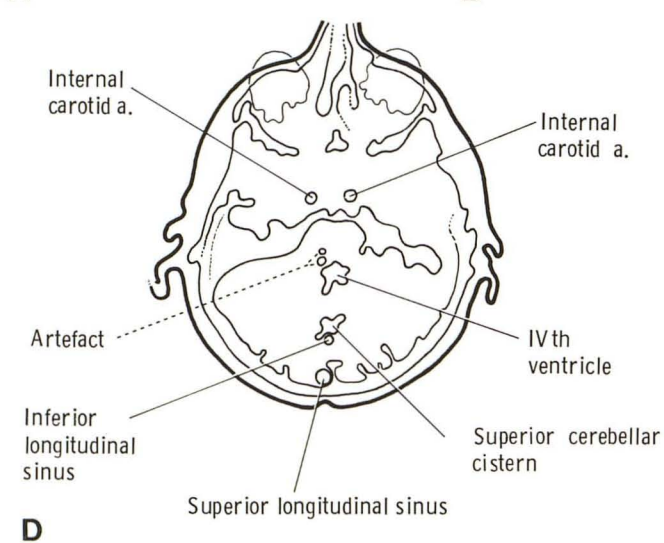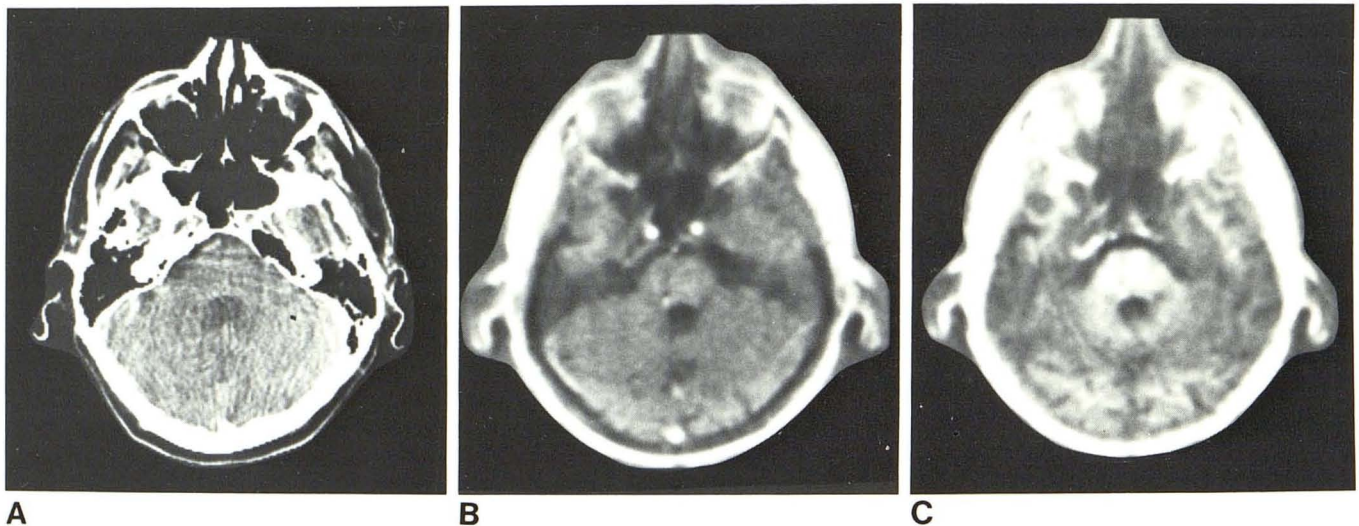spin-echo scan (**C**, *arrows*).

A

B

C

Internal
carotid a.

Internal
carotid a.

Artefact

IVth
ventricle

Inferior
longitudinal
sinus

Superior cerebellar
cistern

Superior longitudinal sinus

D

Fig. 6.—CT (**A**), saturation-recovery (**B**), and inversion-recovery (**C**) scans
of upper pons. Fourth ventricle is seen on all scans. Internal carotid artery,
basilar artery, and longitudinal sinuses seen on saturation-recovery scan (**B**).
D, Key diagram.

the middle fossa on the saturation-recovery scan unobscured by artifact. The internal carotid arteries and the basilar artery appear as clearly defined white areas on the scan. The superior longitudinal sinus is also seen posteriorly, and part of the margin of the transverse sinus is seen laterally on the left. The inferior longitudinal sinus is seen posterior to the superior cerebellar cistern. In the inversion-recovery scan, gray and white matter are clearly differentiated and gyri are seen within the temporal and occipital poles. The white matter of the pons is seen extending laterally into the cerebellum surrounding the fourth ventricle.

CT, saturation-recovery, and inversion-recovery scans through the pons are shown in figure 7. The saturation-recovery scan shows the peripheral margin of the cerebellum surrounded by transverse sinuses. The internal carotid arteries are seen coursing medially. The inferior aspects of the temporal lobes are seen on the floor of the middle cranial fossa. On the inversion-recovery scan, the middle cerebellar peduncles are clearly seen as large white-matter structures extending posterolaterally from the pons, and the left trigeminal nerve is seen extending anteriorly.

A further inversion-recovery scan through the pons in another subject is shown in figure 8. The middle cerebellar peduncle is seen lateral to the fourth ventricle with the vermis of the cerebellum and the dentate nucleus situated posteriorly. Anterior to the pons, the trigeminal ganglia are seen bilaterally.

Comparable CT and inversion-recovery scans through the medulla oblongata are shown in figures 9A and 9B. The inversion-recovery scan shows the contour of the medulla free of artifacts. Fat is seen as a white area within the orbits on the NMR scan and the lens of the eye is seen within the globe. In a saturation-recovery picture of the medulla (fig. 9C), internal carotid and vertebral arteries are seen as well as the transverse sinuses and the right inferior petrosal sinus.

The base of the brain is shown in figure 10 where CT, inversion-recovery, and spin-echo scans are compared. The inversion-recovery scan shows gray and white matter within the spinal cord. The internal carotid arteries as well as the internal jugular vein and bulb are seen as dark areas (see fig. 10D). Muscle and fat are seen in corresponding positions on CT and the inversion-recovery scan, with fat appearing dark on CT and white on the NMR scans. The spin-echo scan shows the margins of spinal cord with greater clarity than the inversion-recovery scan, although blood vessels are similarly seen as dark areas. Soft-tissue detail is readily visible.

Discussion

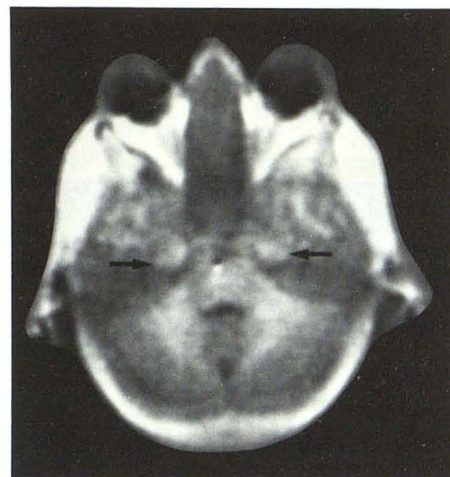In comparison with CT, the NMR images were notable for the absence of linear artifact from bone and for the choice

Fig. 8.—Inversion-recovery scan of pons. Middle cerebellar peduncle extends into cerebellum and trigeminal ganglia seen anterior to pons (arrows).
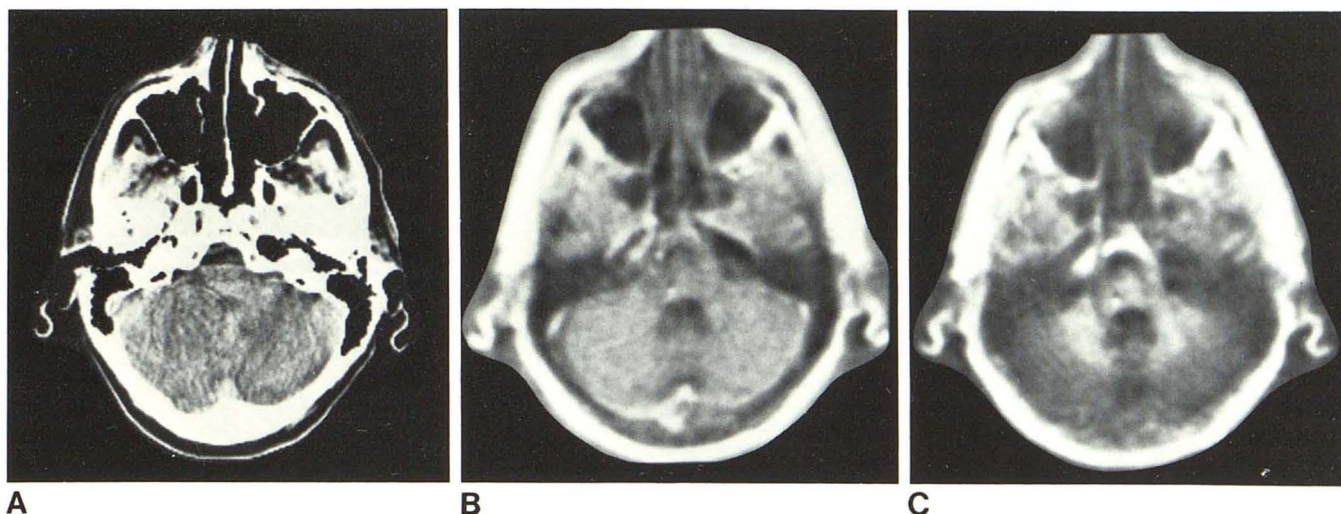
A   B   C

Fig. 7.—CT (A), saturation-recovery (B), and inversion-recovery (C) scans at level of pons. Fourth ventricle seen on all scans. Saturation-recovery scan (B) shows transverse sinuses at margin of cerebellum and internal carotid arteries coursing medially. Middle cerebellar peduncle seen in inversion-recovery scan (C) and fifth nerve extends anteriorly on left.
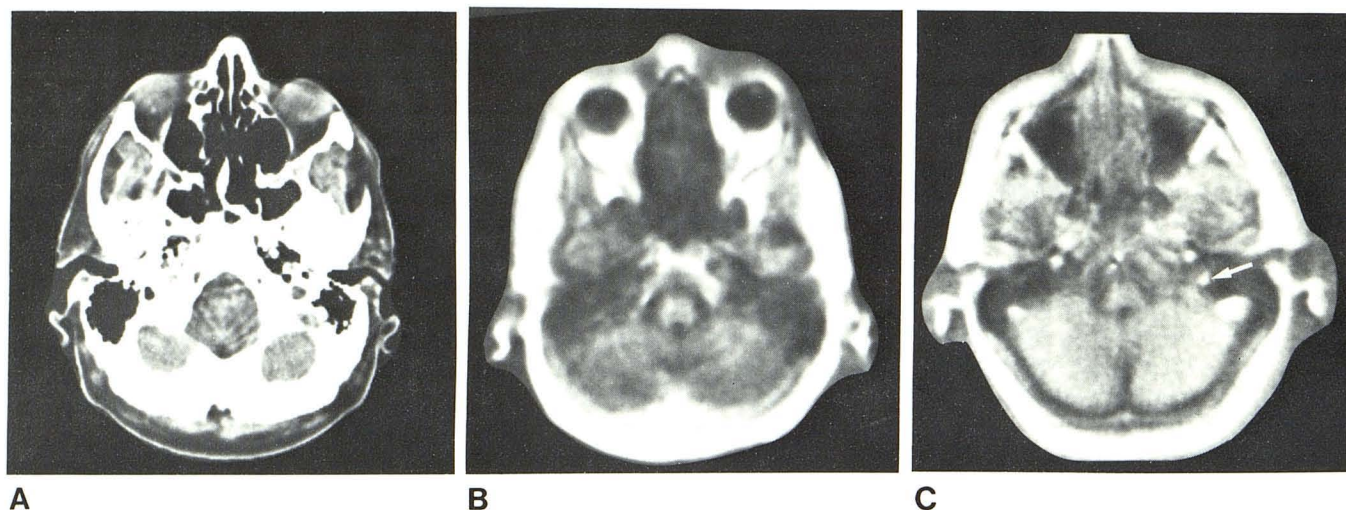
A

B

C

Fig. 9.—CT (A), inversion-recovery (B), and saturation-recovery (C) scans of medulla oblongata. Inversion-recovery scan (B) shows medulla; also globes, lens of eye, and orbital fat. Saturation-recovery scan (C) also shows medulla, with vertebral arteries running medially. Internal carotid arteries and transverse sinuses also seen. Inferior petrosal sinus on right (arrow).

A

B

C

Internal carotid a.

Artefact

Internal jugular v.

Internal carotid a.

Jugular bulb

Mastoid air cells
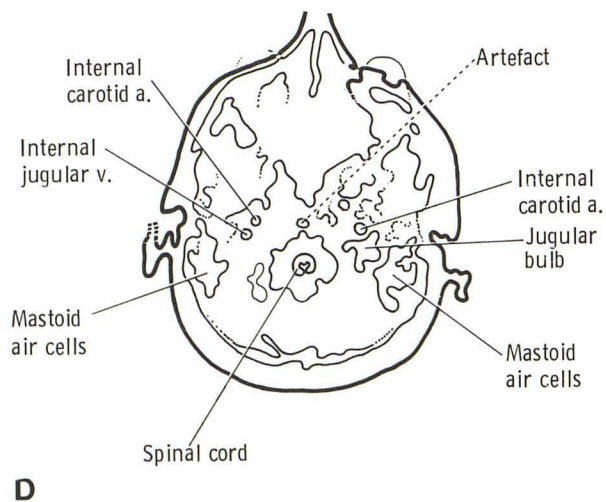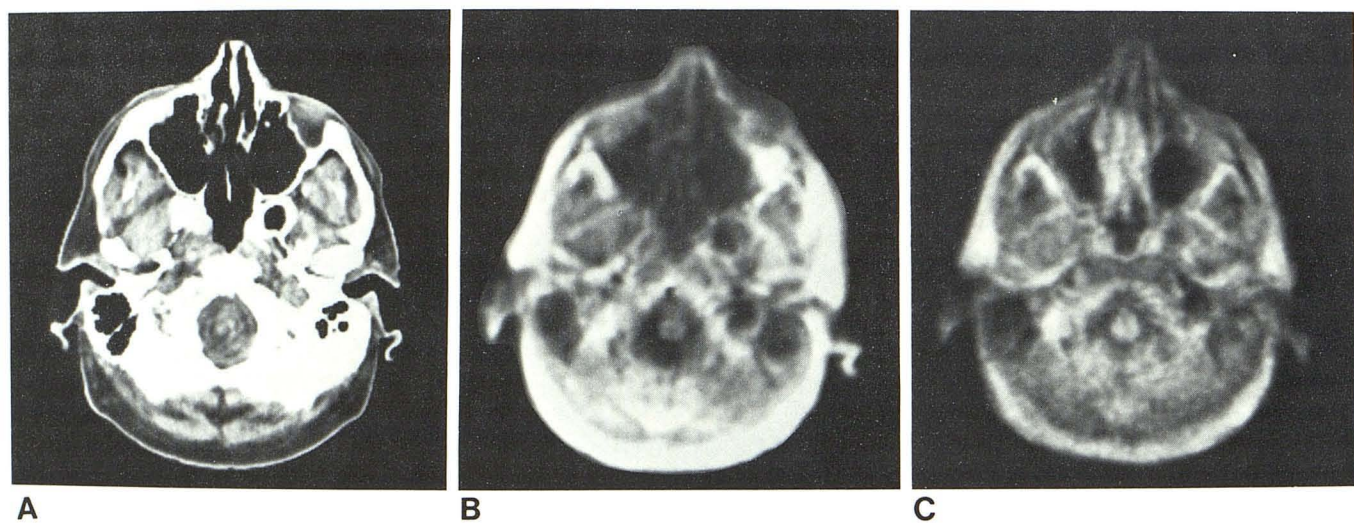
Mastoid air cells

Spinal cord

D

Fig. 10.—CT (A), inversion-recovery (B), and spin-echo (C) scans of base of brain. Inversion-recovery scan (B) shows gray and white matter within spinal cord. Internal carotid arteries and internal jugular veins appear dark. Spin-echo scan (C) shows spinal cord and details of fat muscle and mucosal detail in nasopharynx and infratemporal fossa. D, Key diagram.

of the imaging sequences available with which to demonstrate different anatomic features.

In x-ray CT there is a wide difference in attentuation coefficient between tissues, such as bone and lung, leading to large variation in radiation intensity seen by the detectors; this is an important factor in the production of linear artifacts. In NMR the range of emitted signal values is much less, and comparable linear artifacts are not usually seen except at the skin surface where the greatest change in signal size occurs. Beam-hardening effects may also contribute to artifact production around the bones in x-ray CT, but in NMR the RF field is arranged to fall in the low absorption window of body tissue so that the magnitude and phase of the field is the same at all places in the slice.

Changing the NMR scanning sequence gives a variety of NMR images, each of which contains different information. Saturation-recovery scans may be used not only to demonstrate blood vessels but also to provide measurements of blood flow by varying the scanning rate and sequence.

The gray-white matter differentiation obtained using the inversion-recovery sequence enables the substantia nigra and middle cerebellar peduncle to be visualised. It is possible that this capacity to differentiate gray and white matter may prove to be of considerable value in the diagnosis of the wide range of neurologic diseases in which demyelination is a significant component of the pathologic process.

Experience with spin-echo scanning is limited but while images show little gray-white matter contrast, they do show considerable soft-tissue differentiation at the base of the skull. The order and range of T_2 values for different tissues does not follow exactly that of T_1 values, so that spin-echo images may complement inversion-recovery scans providing additional diagnostic information.

Although each image shown depends on more than one variable, images of T_1 or T_2 alone can be derived from combinations of the above types of image. Such scans are noisier but allow direct measurements of T_1 or T_2 to be obtained when these are required.

The potential of NMR imaging needs little emphasis. Already images comparable with and in several respects superior to those obtained with a new rotate-rotate CT scanner have been produced. The results of clinical evaluation of the above and other NMR machines will be of considerable interest in the future.

REFERENCES

1. Hounsfield GN. Computed medical imaging. *J Comput Assist Tomogr* **1980**;4:665–674
2. Holland GN, Moore WS, Hawkes RC. Nuclear magnetic resonance tomography of the brain. *J Comput Assist Tomogr* **1980**;4:1–3
3. Moore WS, Holland GN, Kreel L. The NMR CAT scanner: a new look at the brain. *CT* **1980**;4:1–7
4. Holland GN, Hawkes RC, Moore WS. Nuclear magnetic resonance (NMR) tomography of the brain: coronal and sagittal sections. *J Comput Assist Tomogr* **1980**;4:429–433
5. Hawkes RC, Holland GN, Moore WS, Worthington BS. Nuclear magnetic resonance (NMR) tomography of the brain: a preliminary clinical assessment with demonstration of pathology. *J Comput Assist Tomogr* **1980**;4:577–586
6. Moore WS, Holland GW. Nuclear magnetic resonance imaging. *Br Med Bull* **1980**;36:297–299
7. Edelstein WA, Hutchinson JMS, Smith FW, Mallard J, Johnson G, Redpath TW. Human whole-body NMR tomographic imaging: normal sections. *Br J Radiol* **1981**;54:149–151
8. Doyle FH, Gore JC, Pennock JM, et al. Nuclear magnetic resonance imaging of the brain. *Lancet* **1981**;2:53–57
9. NRPB exposure to nuclear magnetic resonance clinical imaging 1980. (available from the Secretary, NRPB, Harwell, Oxon OX11 ORQ, United Kingdom)
10. Hahn EL. Spin echoes. *Phys Rev* **1950**;80:580–594